Influence of Water Saturation and Water Memory on CO_2 Hydrate Formation/Dissociation in Porous Media Under Flowing Condition

Aghajanloo, M.; Taghinejad, S. M.; Voskov, D.; Farajzadeh, R.

DOI
10.2118/218824-MS

Publication date
2024

Document Version
Final published version

Published in
Society of Petroleum Engineers - SPE Conference at Oman Petroleum and Energy Show, OPES 2024

SPE-218824-MS

Influence of Water Saturation and Water Memory on CO_2 Hydrate Formation/ Dissociation in Porous Media Under Flowing Condition

M. Aghajanloo and S. M. Taghinejad, Delft University of Technology, Department of Geoscience and Engineering, Delft, The Netherlands; D. Voskov, Delft University of Technology, Department of Geoscience and Engineering, Delft, The Netherlands / Energy, Science and Engineering, Stanford University; R. Farajzadeh, Delft University of Technology, Department of Geoscience and Engineering, Delft, Shell Global Solutions International B.V., The Netherlands

 DOI 10.2118/218824-MS

This paper was prepared for presentation at the SPE Conference at Oman Petroleum & Energy Show held in Muscat, Oman, 22 - 24 April 2024.

Abstract

Injection of high-pressure CO_2 into depleted gas reservoirs can lead to low temperatures promoting formation of hydrate in the near wellbore area resulting in reduced injection rates. The design of effective mitigation methods requires an understanding of the impact of crucial parameters on the formation and dissociation of CO_2 hydrate within the porous medium under flowing conditions. This study investigates the influence of water saturation (ranging from 20% to 40%) on the saturation and kinetics of CO_2 hydrate during continuous CO_2 injection. The experiments were conducted under a medical X-ray computed tomography (CT) to monitor the dynamics of hydrate growth inside the core and to calculate the hydrate saturation profile. The experimental data reveal increase in CO_2 hydrate saturation with increasing water saturation levels. The extent of permeability reduction is strongly dependent on the initial water saturation: beyond a certain water saturation the core is fully blocked. For water saturations representative of the depleted gas fields, although the amount of generated hydrate is not sufficient to fully block the CO_2 flow path, a significant reduction in permeability (approximately 80%) is measured. It is also observed that the volume of water+hydrate phases increases during hydrate formation, indicating a lower-than-water density for CO_2 hydrate. Having a history of hydrate at the same water saturation leads to an increase in CO_2 consumption compared to the primary formation of hydrate, confirming the existence of the water memory effect in porous media.

Keywords: Water Saturation, Porous Media, Hydrate Formation/Dissociation Cycle, Memory Effect, CO_2 Hydrate kinetic, Permeability, X-ray CT scan

Introduction

Carbon dioxide (CO_2) emissions from anthropogenic sources are a major contributor to the rapid rise in global temperature and the subsequent effects of climate change, which will indeed have substantial implications for future life on Earth (Benson & Cole, 2008; House et al., 2006; Nunes, 2023). Considering the ongoing reliance on fossil fuels for energy generation, the adoption of carbon capture and storage (CCS) is increasingly acknowledged as a highly promising technology to mitigate the environmental impacts of CO_2 emissions (Ketzer et al., 2012; Roy et al., 2023).

Among the diverse geological formations applicable for CO_2 storage, gas-depleted fields hold distinct advantages and offer substantial secure and long-term storage capacity (Bachu, 2000; Dance, 2013; Oldenburg & Benson, 2002; Underschultz et al., 2011). Nevertheless, in depleted low-pressure reservoirs, the introduction of high pressure condensed CO_2 during injection can lead to substantial adiabatic expansion, a phenomenon known as Joule-Thomson cooling (JTC), particularly within the well-tubing or the near wellbore region. This is mainly attributed to the establishment of significant pressure gradients (Oldenburg, 2006). A notable concern associated with this phenomenon is the potential for CO_2 hydrate generation when CO_2 interacts with the residual water during the injection phase (Wapperom et al., 2022; Hoteit et al., 2019). This CO_2 hydrate formation pose flow assurance challenges and potentially compromise the functionality of the injection well (Aghajanloo, 2023; Chesnokov, 2023).

Many publications on CO_2 injection in depleted gas reservoirs have addressed different aspects on the CO_2 phase transition (CO_2 hydrate formation) within the wellbore such as impact of CO_2 flow characteristic (Hoteit et al., 2019), CO_2 pretreatment (Le Goff, 2021), salinity of formation water (Sun & Englezos, 2016), salt precipitation (Akindipe et al., 2022; Hansen et al., 2013), and rock mineralogy and permeability (Gauteplass et al., 2020), aiming to assess and mitigate this operational risk. Nevertheless, there has been no exploration into how reservoir water content (water saturation), and the water memory (refers to the phenomenon where previous hydrate formation experiences an impact on subsequent nucleation) impact the CO_2 hydrate formation and saturation under flowing conditions (Singh et al., 2020). Research demonstrate that at high water saturations region, where the porous medium is predominantly filled with water (>90%), the formation of gas hydrates can be constrained due to the limited availability of a gas phase (Wang et al., 2022). Conversely, low water saturations with substantial gas content are more favorable for gas hydrate formation (Ge et al., 2019). To assess the feasibility of CO_2 storage in depleted reservoirs, quantifying the impact of different water saturations in the presence/absence of water memory on CO_2 hydrate volume/saturation is required to identify under which condition hydrate is more stable and the effect of hydrate on injectivity becomes detrimental for CCS projects (Wei & Maeda, 2023).

Hence, the aim of this study is to present insights into the influence of low water saturation ranges on the volume of CO_2 hydrate and the resulting permeability changes in a Bentheimer sand core. The core flood experiments were conducted under isothermal condition of 273.65 K, with the initial pressure set at 3 MPa. The study also provided an opportunity to assess whether the water memory can influence the kinetics of CO_2 hydrate such as CO_2 consumption rate and induction time within porous media. Furthermore, the study applied X-ray CT scanning to characterize and quantify water/hydrate saturation and distribution along the core during dynamic CO_2 injection, particularly at three initial water saturation levels.

Experimental Section

Material

The CO_2 as hydrate former and N_2 had a certified purity respectively 99.7% and 99.999%, were sourced from Linde Co. gas supplier. The electrolyte (NaCl) was of certified 99.5-grade provided by Fisher Scientific. Deionized distilled water was used to prepare the brine solutions. Cylindrical outcrop Bentheimer core plugs were used as porous media in all the experiments. These core rock had dimensions of 3.8 cm in diameter, 17 cm in length, a porosity (φ) of 0.23, and permeability (K) ranging from 2.2 to 2.5 D.

Experimental Setup

The schematic of the experimental setup applied for core-flood experiments is depicted in Fig. 1. This includes a Bentheimer sand rock coated with a 5mm thick layer of epoxy resin to provide a protective barrier for the fluids. The sand core is located inside a polyether ether ketone core holder, which is designed to maintain containment at high pressure and low temperature. Four pressure transducers are employed to measure pressure changes at the: inlet, 2.25 cm from the inlet, 6.5 cm from the outlet, and outlet (GE UNIK 5000— Accuracy to ±0.04% Full Scale, ranges from 0.007 to 8 MPa). Two differential pressure devices (Endress and Hauser, Deltabar S, ranges: -0.03 to +0.03 MPa) are utilized to acquire the pressure difference at the other two locations. Two thermocouples are placed inside the core and at the core outlet to measure local temperatures. A high-pressure control system, typically referred to as the back pressure system, is linked to the outlet of the core holder. The back pressure is adjusted with a large N_2 cylinder to sustain the specific pressure of the experiments (3MPa). The effluent solution is accumulated in an adsorbent-equipped vessel. A data acquisition system is responsible for collecting and adjusting various parameters such as temperature and pressure within the system. This includes a pulse-free high-precision piston pump (Quizix QX-6000HC) for driving solutions from the vessel into the core holder and a high-pressure gas mass flow controller (Bronkhorst F-230M) to manage the injection rate of gas flowrate. The inlet line between the pumps and the inlet end-cap is kept long to equilibrate the water and gas before entering the core. The effluent is collected in a 500 ml collection vessel. The core holder is enveloped by a cooling jacket where the cooling medium is continuously circulated through the jacket using a circulator (LAUDA Proline RP845). The precision of the circulator is within ±0.1 °C. A medical X-ray CT-scan instrument (Siemens Somatom Volume) is used to compute fluid saturation levels and hydrate volume during the formation/dissociation process. The slice thickness for each scan is 0.6 mm, while a resolution of 0.2 mm in the other two dimensions, leads to a voxel size of 0.2 * 0.2 * 0.6 mm^3. A voltage of 140 kV and a current of 250 mA is employed.

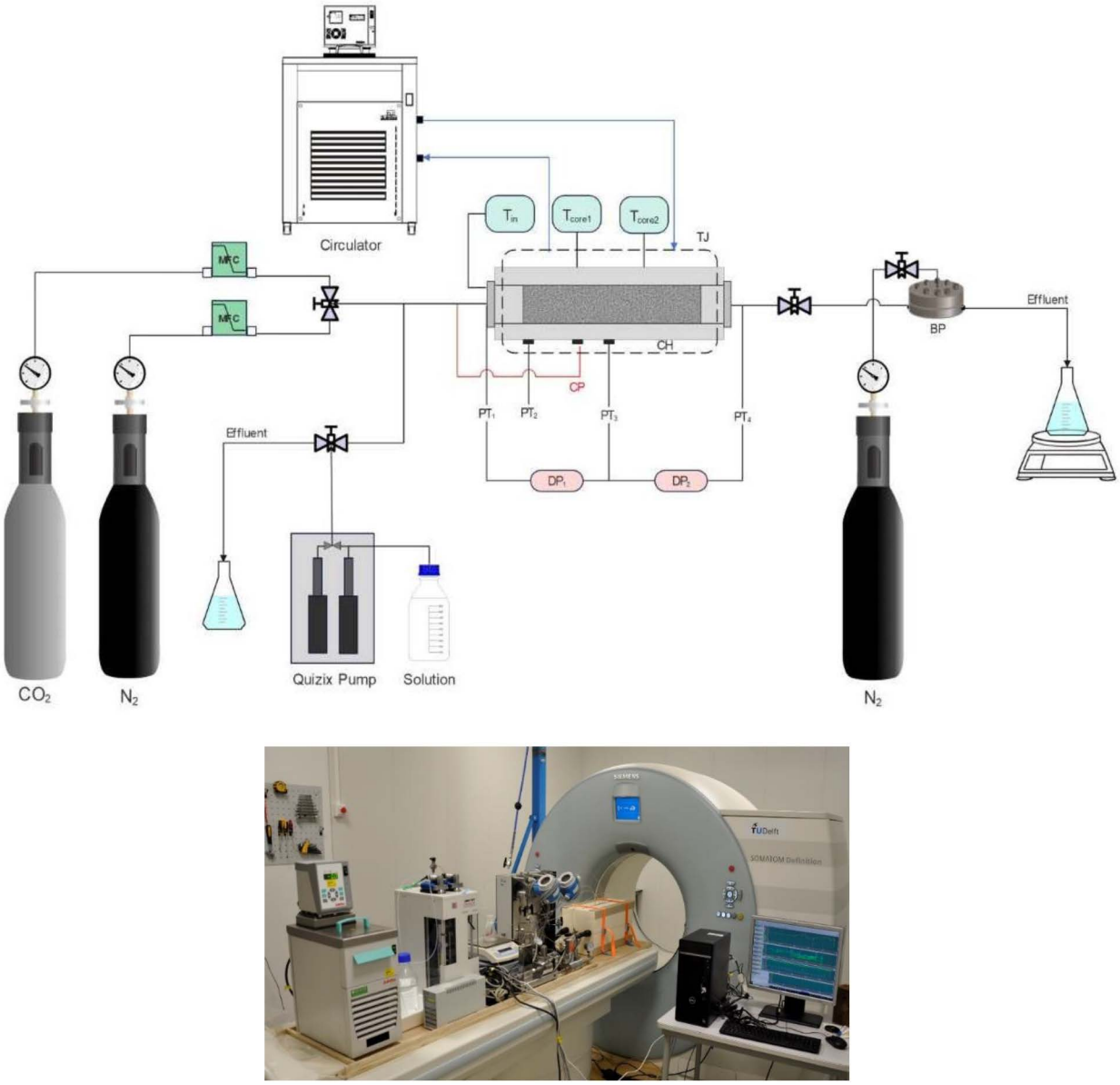

Figure 1—Schematic diagram and photo of the laboratory apparatus. (BP) Back Pressure; (CH) Core Holder; (CP) Confining Pressure; (DP) Differential Pressure; (MFC) Mass Flow Controller; (PT) Pressure Transducer; (TC) Thermocouple; (Boon & Hajibeygi) Thermal Jacket

Experimental Procedure

Water Saturation. The experiments involved the measurement of water saturation, hydrate nucleation time and hydrate saturation by conducting core-flood tests on a homogenous Bentheim sandstone. To quantify the water/hydrate distribution within the rock core, a medical X-ray CT scanner was employed. To achieve a uninform water saturation below 40% in the core, a modified gas/water co-injection technique was employed (Eftekhari & Farajzadeh, 2017). In brief, the process began with the injection of N_2 into the system, gradually rising the pressure by 0.5 MPa increments up to a target pressure of 3 MPa. Confining pressure was set equal to the injection pressure. Subsequently, a degassed solution consisting of 1 wt% NaCl and deionized water with N_2 was simultaneously introduced into the vertical core using a specific fractional flow under constant temperature of 273.65 K. The total flow rate, which included both gas and liquid flow, was maintained at 6 ml/min. The ratio of brine to N_2 was regulated using a Quizix pump and a mass flow controller.

Hydrate Formation/Dissociation Cycle. Following the establishment of the desired water saturation, CO_2 injection into the core commenced at a constant velocity of 1 ml/min. The initial pressures selected for hydrate formation in all experimental runs were set at 3MPa, while the temperature was maintained at 273.65±0.5 K (~6 degree of subcooling based on CO_2/water P-T phase diagram shown in Fig. 2). This consistent temperature and pressure were chosen to create a controlled environment closely resembling real-reservoir conditions where CO_2 hydrates can potentially form. This allowed for precise observations and measurements of CO_2 hydrate behavior under specific operating conditions. Cyclic tests were conducted to investigate whether the presence of water memory influences subsequent hydrate nucleation.

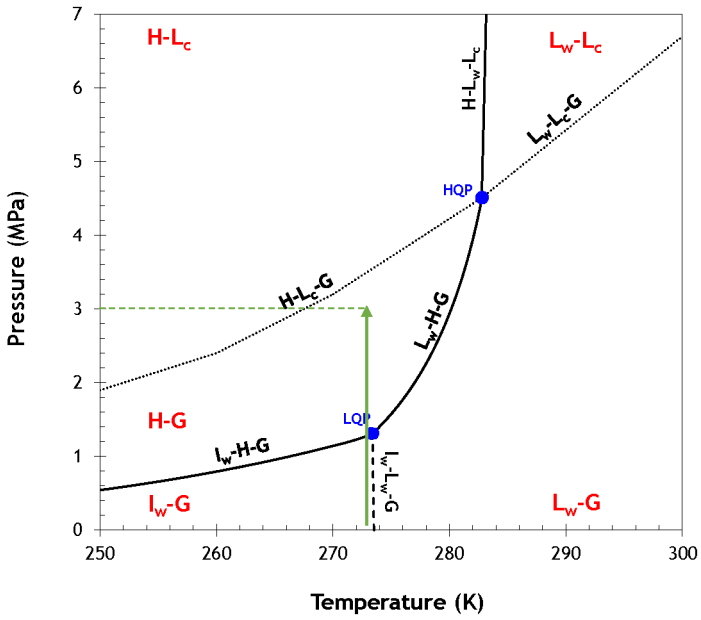

Figure 2—Three-phase diagram of the CO_2-water mixture. The symbols I_w, L_c, L_w, H, and G represent ice water, liquid CO_2, liquid water, hydrate, and gas, respectively. HQP and LQP refer to high (L_wHL_cG) and low (I_wHL_WG) quadruple points. The smooth line represent the three-phase equilibrium line, the dotted line indicate the CO_2 condensed line, and the dashed line is ice line.

The experimental procedure encompassed CO_2 hydrate formation until a steady state was achieved, after which dissociation was initiated. The first three cycles involved thermal stimulation to dissociate the existing hydrate, while for some tests the fourth cycle used a solution containing methanol (MeOH) to decompose the hydrate structure. Chemical solutions were prepared at loadings of 15 wt% MeOH with degassed and deionized water containing 1 wt% NaCl. During hydrate dissociation via thermal stimulation, the temperature remained below 293.15 K, and the dissociation process was completed within a day to avoid eliminating the hydrate memory of water.

CO_2 Consumption and Hydrate Formation Rate

The data acquisition system recorded the pressures and temperatures inside the core sample every 10 second. The calculated CO_2 consumption (total moles of CO_2 consumed from the gas phase) at any given time (t) was determined as a function of the compressibility factor. The calculations were made based on an assumption regarding gas consumption (Δn), which was defined as the difference in the amount of CO_2 introduced into the core at time t (n_t) and the amount of CO_2 that exited the core at next time step ($n_t+\Delta t$). This estimation can be expressed as follows:

$$n_t = \left(\frac{PV}{ZRT}\right)_t \tag{1}$$

$$\Delta n = \sum_0^t \left(n_t - n_{t-\Delta t}\right) \tag{2}$$

where P represents the pressure inside the core, V stands for gas volume, T is the temperature, and the universal gas constant is expressed as R. The compressibility factor (z) was calculated iteratively through the Cubic-Plus-Association (CPA) equation of state (EoS) using HydraFLASH software version 3.8. In equation 2, t=0 denotes the initial condition (just before the CO_2 injection), and t>0 represents time during CO_2 injection.

From kinetic perspective, the CO_2 hydrate formation process encompasses the diffusion of dissolved gas from the aqueous phase to the interface of the hydrate crystal and brine, where the CO_2 molecules are integrated into the clathrate structure. To quantify the rate of CO_2 hydrate formation in dynamic conditions, the moles of CO_2 consumed were utilized. The rate of change in CO_2 gas moles at each time yields the formation rate. This was computed using the following equation:

$$r_{CO_2} = \left(\frac{dn_t}{dt}\right)_{t-\Delta t,t} \tag{3}$$

Where r is the CO_2 hydrate formation rate. Δn is the difference in the number of moles of CO_2 gas. Δt is the time interval.

CO_2 Hydrate Saturation

The total mass of hydrate formation (Dhamu et al., 2023) was obtained applying following equation:

$$m_H = f_{conv} \times n_{H_2O}\left[Mw^{H_2O} + \frac{Mw^{CO_2}}{NH}\right] \tag{4}$$

where f_{conv} is the fraction of water converted to hydrate, n_{H_2o} is the total moles of water inside the core, and Mw^{H_2o} and Mw^{CO_2} are water and CO_2 molecular weight, respectively. Hydration number (NH) is the average number of water per gas molecule in a hydrate unit.

Hydrate saturation (S_H), was determined by calculating the volume of hydrate normalized to the pore volume of the core (V_φ). This calculation was carried out using the following equation:

$$S_H(\%) = \frac{V_H}{V_\varphi} = \frac{m_H}{V_\varphi \times \rho_H} \tag{5}$$

where V_H and ρ_H is the volume and density of hydrate defined by the following relationship:

$$\rho_H = \frac{m_H}{V_H} \tag{6}$$

To calculate water and hydrate saturations (Boon & Hajibeygi, 2022), CT images of the core were obtained under both fully brine-saturated (CT_{wet}) and dry (CT_{dry}) conditions. The saturation was calculated using the following equation (Lei & Seol, 2019):

$$S_{w/H} = \frac{CT_{exp} - CT_{dry}}{CT_{wet} - CT_{dry}} \tag{7}$$

where, CT_{exp} is the voxel level CT number for the core at a specific step during CO_2 injection (hydrate formation).

Result and Discussion

Impact of Water Saturation and Water Memory on the CO_2 Hydrate Saturation

A significant risk to injectivity during CO_2 storage is the potential for hydrate formation near wellbore area. Consequently, when investigating the impact of hydrate, multiple factors need to be considered, including thermodynamic condition (T and P), salinity, and water saturation (J. Wang et al., 2022). Depleted gas reservoir typically exhibit low water saturations; however, aquifer influx and water mobilized by capillary pressure can pull back water near wellbore area. Moreover, in a heterogeneous reservoir different layer may

contain different levels of water saturation. Hence, it is essential to quantify impact of water saturation on extent of injectivity decline and dynamics of hydrate formation/dissociation.

To gain insight into the experimental findings, the initial step involved prediction of hydrate saturation corresponding to water saturations ranging from 20% to 60% at 3 MPa using HydraFLASH software, applying the CPA EoS. Fig. 3 presents the linear correlation between hydrate saturation and water saturation. The slope of the line in this figure is calculated to be 1.21, with >0.96% water-to-hydrate conversion efficiency, indicating that hydrate occupies 21% more volume compared to water under assumed conditions. With hydration number of ~5.9 to 6.1, the estimated hydrate density is ~0.804 g/ml. This estimation ignores coexistence of ice with the hydrate at -10 °C. Accordingly, in the studied range of water saturations (20%-60%, when excess CO_2 is present, the efficiency of water-to-hydrate conversion remains constant across the specified water saturation levels. However, as depicted in Fig. 4, under a constant pressure of 3 MPa, the latent heat (enthalpy) of CO_2 hydrate formation decreasing from 396.7 kJ/kg with water saturation above 20%. Additionally, the influence of water saturation on hydrate saturation is different when hydrate coexists with ice at lower temperatures. The simulation results also indicate that when the reservoir conditions are situated within the hydrate stability region, at a constant pressure the temperature has a relatively low impact on hydrate saturation during CO_2 injection. This limited influence of temperature can be attributed to the constant density of CO_2 in the gas phase (due to continuous CO_2 injection), leading to the saturation of water with CO_2. Consequently, the hydrate lattice stabilizes upon achieving maximum CO_2 filling. Consequently, additional temperature change does not significantly alter the encapsulation of CO_2, a crucial factor for hydrate stabilization. For these calculations, at S_w=0.81, hydrate will fully occupy the porous medium. However, flow of CO_2 will be hindered if hydrate saturation reaches a specific value and therefore formation of hydrate will be limited due to inaccessibility of CO_2.

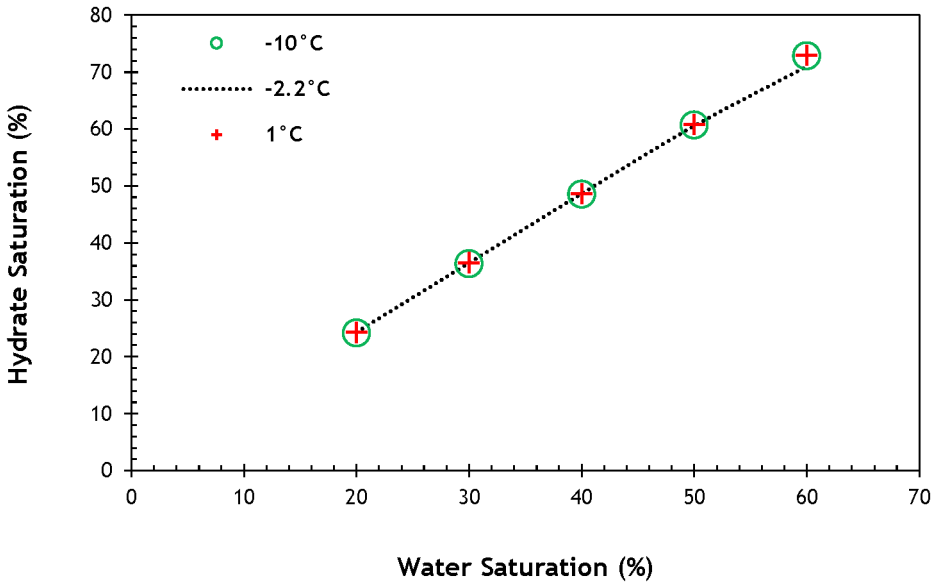

Figure 3—Relation between water saturation and hydrate saturation at P=3 MPa for different temperatures. At T=263.15 K, no ice formation was assumed. The density of the hydrate was calculated as 0.803±0.0001 g/ml. (HydraFLASH version 3.8, CPA EoS)

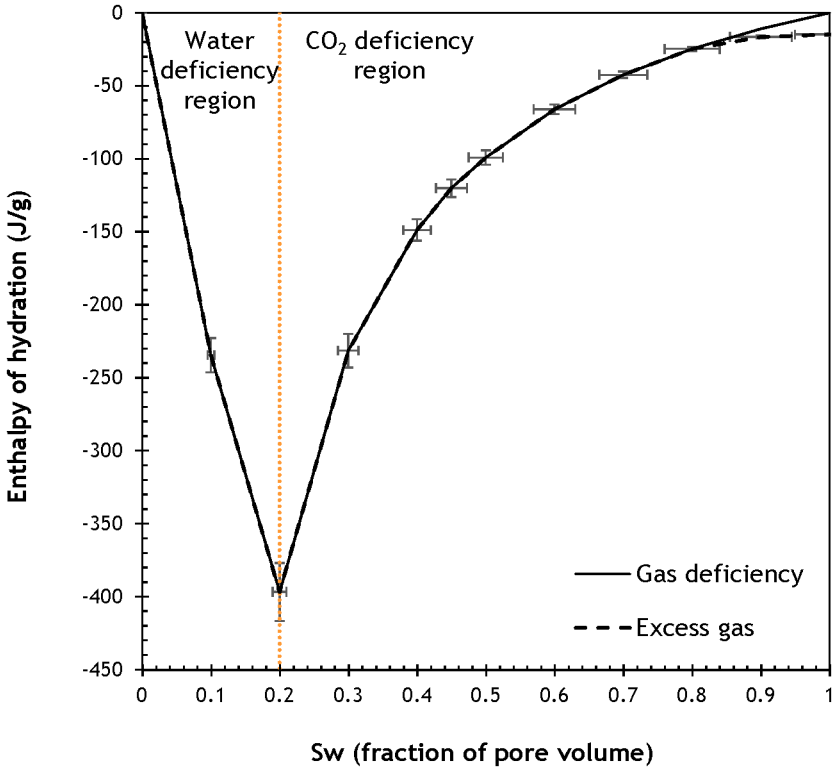

Figure 4—Latent heat of hydrate formation in different water saturation at P=3 MPa in presence/absence of excess CO_2. (HydraFLASH version 3.8, CPA EoS)

Fig. 5 depicts the pressure and temperature data from a sample experiment of 41.2% water saturation (E8). CO_2 injection commenced in the first cycle following the saturation of the sand core with 1wt% NaCl brine. The primary sign of hydrate formation was macroscopically detected at induction time, characterized by a simultaneous pressure drop due to CO_2 encapsulation within the hydrate cavities and a temperature increase resulting from the exothermic hydrate formation reaction (around 1 hr in the first cycle). Following the induction period, pressures gradually increased, corresponding to the progress in hydrate growth during CO_2 injection. Despite this volume increase causing a reduction in porosity and permeability, leading to increased pressure, no blockage was recorded under these conditions. Moreover, this pressure increase also be attributed to the ongoing CO_2 injection, which resulted in hydrate cages trapping more CO_2 and thereby enhancing the stability of the hydrate structure. CO_2 injection persisted throughout each cycle until the thermodynamic conditions (P and T) reached a steady state. Thermal stimulation at 293.15 K was employed to dissociate the hydrate. Following the hydrate dissociation of the first cycle, water saturation decreased to 39.6%, due to the production of 0.71 ml of water from the core (see Table 2). Subsequently, the system was cooled during N_2 injection, and the N_2 stream was replaced by the CO_2 upon reaching the desired subcooling (~6 degree of subcooling) to induce hydrate formation of the next cycle.

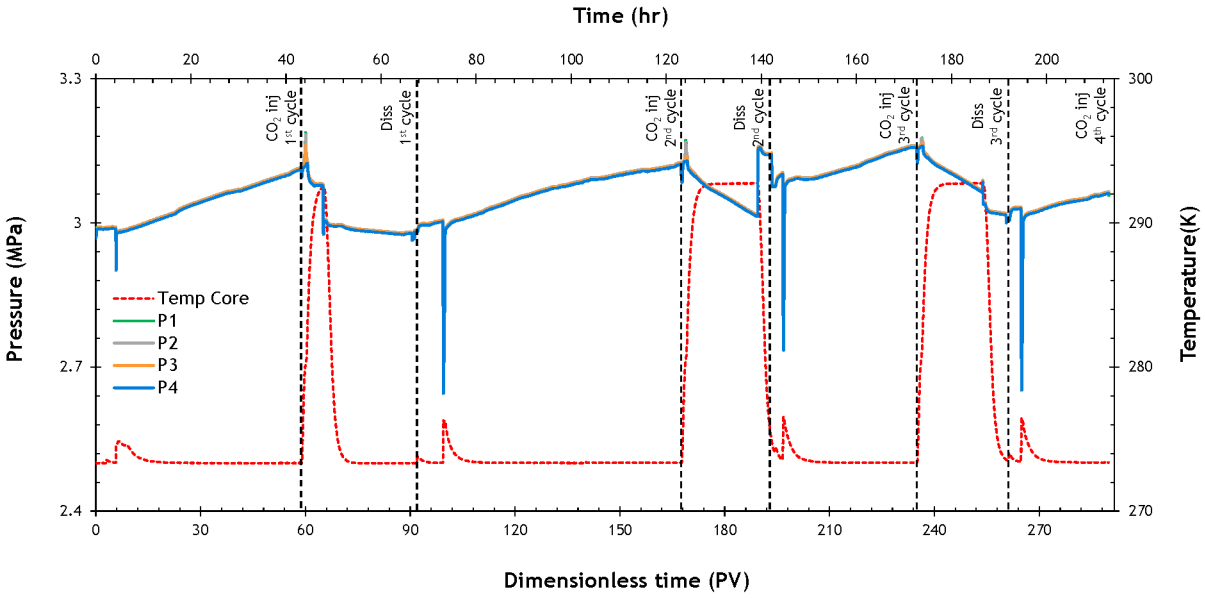

Figure 5—Pressure and temperature change during CO_2 hydrate formation and dissociation cycle for Sw=42.1% containing 1wt% NaCl. Initial condition: 3MPa; and 273.65K. Pressure changes were monitored at the inlet (P_1), 2.25 cm from the inlet (P_2), 6.5 cm from the outlet (P_3), and the outlet (P_4).

Analysis of data from the four cycles (details reported in Table 2) indicated that the first cycle exhibited a significantly lower pressure drop at induction time (0.09 MPa) compared to subsequent cycles (approximately 0.36 MPa). This difference was attributed to the water memory effect, arising from the extensive release of CO_2 encapsulated within hydrate cages during the first hydrate dissociation, leading to the generation of gas bubbles. These CO_2 bubbles contributed to the sharpest pressure drop during subsequent hydrate pore filling. However, despite these pressure variations, final hydrate volume calculations based on water saturation levels did not indicate substantial differences across cycles.

Table 1 provides relevant data from four cycles of hydrate formation for five different distinct water saturations. The most significant pressure drop arising from the onset of hydrate formation (macroscopic induction time) was observed in the fourth cycle of E1, characterized by the lowest water saturation. The result implies that within the studied range of water saturation, the water saturation level of 22% forms a more stable structure of CO_2 hydrate. This criticality might be attributed to a more uniform water distribution at this specific water saturation level, resulting in an improved water-gas interface and an increased dissolution of CO_2. From another perspective, under the specified conditions (273.65K and an initial pressure of 3MPa, in the presence of water memory), the higher-pressure reduction observed in the fourth cycle contributes to the generation of a more stable hydrate, filled with the highest amount of CO_2. In this context, E3 with 30.1% water saturation, demonstrated the longest induction time across all cycles. This observation suggests that at this specific water saturation level, the hydrate nucleation process took the longest time compared to other saturation levels. Moreover, a positive correlation between the induction times (whether fresh or from memory) and the hydrate saturation was evident in the obtained data. However, with an increase in water saturation, blockages in flow channels became apparent in certain secondary cycles, such as the second and third cycles in E5. This phenomenon led to a decline in permeability, confirming that the likelihood of blockage increases with hydrate re-formation. This could be attributed to the redistribution of water following hydrate dissociation. The pressure data recorded along the core length revealed that the blockage occurred in the end section of the core rock, which is likely associated with higher water saturation in that section due to displacement of water by CO_2. Based on the data provided in Table 1, slight variations in hydrate saturation (water-to-hydrate conversion) were observed among cases. However, across all water saturations, there was a consistent increase in conversion from the first cycle, which can be

related to the memory effect. This implies that water memory not only accelerates hydrate nucleation but also influences hydrate density, possibly due to the residual structure hypothesis (Sloan, 1998) and the guest supersaturation hypothesis (Rodger, 2000). Furthermore, findings show that during the primary hydrate formation, the synthesized CO_2 hydrate mainly occupies small pores, while in the secondary synthesis, it enters both small and large pores (Wen et al., 2021). As a result, the CO_2 hydrate previously formed in the larger pores can impede the water in smaller pores from participating in the CO_2 hydrate formation process, creating a pore-blocking effect that was not observed in the second synthesis. Consequently, the calculated hydrate density was lower for the first cycle compared to the subsequent cycles.

Table 1—Summary of phase saturations and hydrate formation results from five distinct water saturation at 273.65K and initial pressure of 3MPa

Water saturation (%)	Water conversion[a] (%)	Induction Time (hr)	Temp change by hydrate formation	CO_2 hydrate saturation[b]	Blockage due to hydrate formation	CO_2 hydrate volume (ml)
E1,1 (22.1)	74.4	0.86	1.97	19.8	-	8.80
E1,2 (19.9)	87.2	1.47	2.11	21.0	observed	9.25
E1,3 (19.9)	89.7	1.33	2.53	21.6	-	9.53
E1,4 (19.9)	95.5	3.17	3.06	23.0	-	10.12
E2,1 (25.9)	58.7	1.72	1.65	18.4	-	8.11
E2,2 (25.9)	76.9	1.33	1.38	24.1	-	10.64
E2,3 (25.9)	83.3	2.25	2.37	26.1	-	11.52
E2,4 (25.9)	77.9	1.08	2.01	24.4	-	10.74
E3,1 (30.1)	61.8	2.72	1.26	22.5	-	9.91
E3,2 (30.1)	90.6	5.94	3.07	33.0	-	14.56
E3,3 (30.1)	90.9	5.58	3.06	33.1	-	14.59
E3,4 (30.1)	91.4	11.28	2.27	33.3	-	14.70
E4,1 (32.2)	70.8	0.42	1.56	27.6	-	12.16
E4,2 (32.2)	87.5	1.33	2.45	34.1	-	15.04
E4,3 (32.2)	86.5	0.97	2.30	33.7	-	14.86
E4,4 (32.2)	92.7	6.89	3.08	36.1	-	15.9
E5,1 (35.1)	61.0	0.92	1.12	25.9	-	11.41
E5,2 (35.1)	85.9	0.58	3.11	36.5	observed	16.08
E5,3 (35.1)	63.3	0.33	2.78	26.9	observed	11.85
E5,4 (35.1)	89.9	1.75	3.32	38.2	-	16.83

[a] hydration number = 6.2

[b] hydrate density ~ 0.803 g/ml

Table 2—Water saturation and CO_2 hydrate formation data with 1ml/min CO_2 injection at 273.65K and initial pressure of 3MPa through the CT-scan

water saturation (%)	Induction Time (hr)	Temp change by hydrate formation	Pressure drop by hydrate formation	CO_2 hydrate saturation[a] (%)	CO_2 hydrate volume (ml)
E6,1 (24.3)	3.97	1.42	0.85	38.7	12.88
E6,2 (24.4)	0.89	1.49	3.58	37.7	12.92
E6,3 (24.2)	0.39	1.54	3.66	37.4	12.83
E6,4 (24.3)	3.69	1.39	3.78	37.9	12.88
E7,1 (35.7)	0.72	1,85	0.16	48.5	18.80
E7,2 (31.4)	1.86	2.34	3.34	45.0	16.62
E7,3 (31.5)	2.33	2,90	4.47	46.8	16.73
E7,4 (31.4)	4.86	3.11	7.15	46.4	16.67
E8,1 (41.2)	5.00	1.48	56.4	54.7	21.89
E8,2 (39.6)	5.92	2.95	49.2	47.7	21.04
E8,3 (39.4)	2.14	2.99	49.9	48.4	20.93
E8,4 (39.5)	3.08	3,05	50.7	49.2	20.98

[a] based on HydraFLASH prediction >97% water to hydrate conversion was assumed

As depicted in Fig. 6, it was observed that for cycles with identical initial water content, the average rate of secondary CO_2 consumption due to CO_2 dissolution and hydrate formation was 2.5 to 4 times greater than that observed in the primary formation. This trend was particularly pronounced at higher water saturations. To clarify, except for water saturations at 22% and 25%, in all cases, the moles of CO_2 consumed were 1.5 times greater than in freshwater (the first cycle with no hydrate history). These findings suggest the presence of water memory during multicycle synthesis processes. Moreover, the findings reveal that during the primary synthesis, CO_2 predominantly occupies small pores, while in the secondary synthesis, it enters both small and large pores (Wen et al., 2021). As a result, the CO_2 hydrate formed in the first cycle could exhibit a slightly lower density compared to the hydrate formed in the secondary synthesis. This difference in pore occupancy and distribution contributes to the observed density difference between the two synthesis cycles. The memory effect of hydrates has been elucidated through the proposal of various mechanistic hypotheses, including the residual structure hypothesis (Sloan et al., 1998; Thompson et al., 2006) and the guest supersaturation hypothesis (Rodger, 2000). Based on the residual structure hypothesis, it is assumed that after a cycle of formation and dissociation, the remaining structure retains the structural features of the hydrate phase. These residual cage structures serve as nucleation sites for the subsequent hydrate synthesis. However, the supersaturation hypothesis refers that by hydrate dissociation, dissolved gas molecules have a sufficiently small size, and the local pressure is sufficient to support gas bubble generation. The presence of these gas bubbles facilitates the nucleation process for the subsequence hydrate formation (Wen et al., 2021).

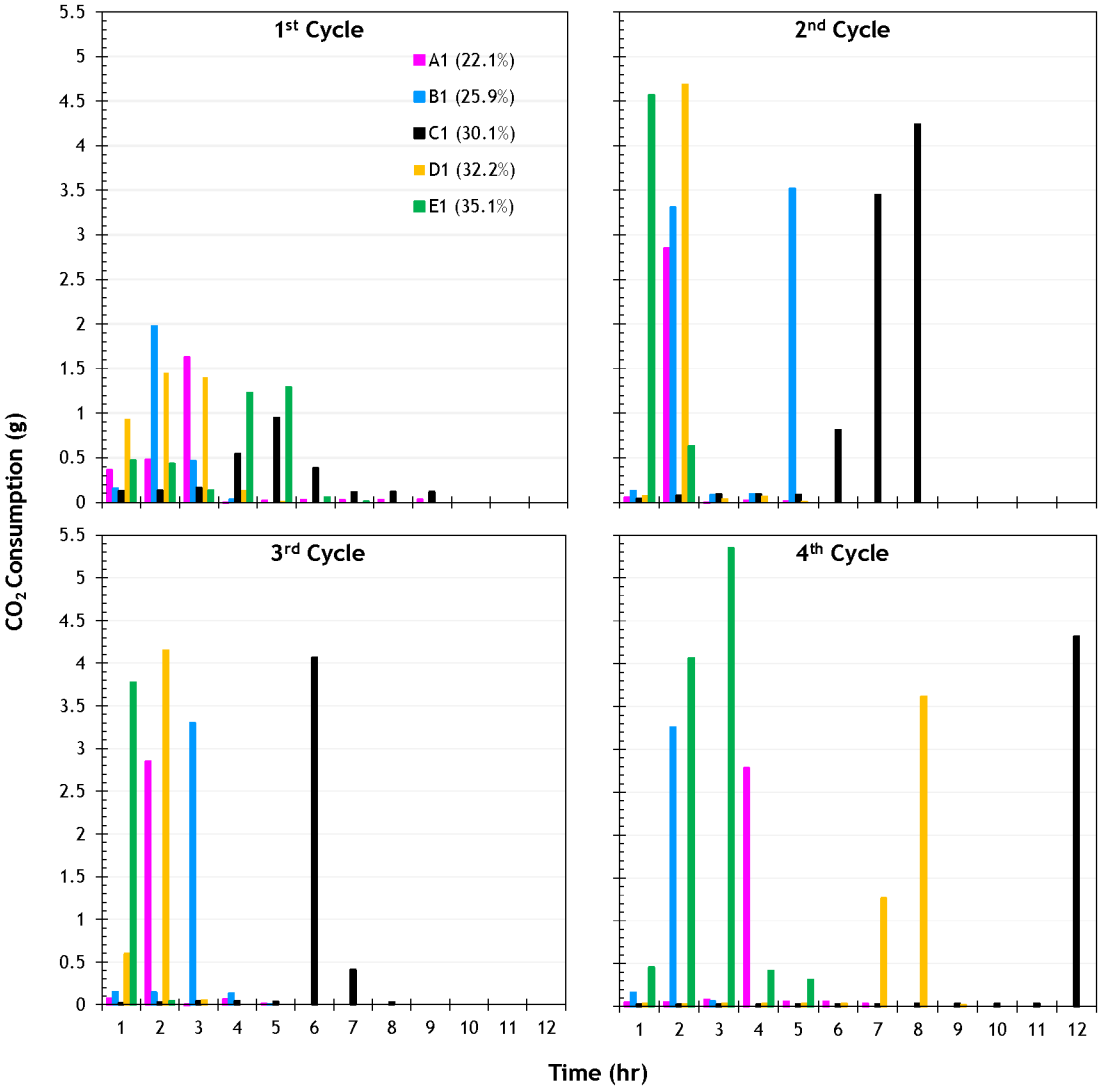

Figure 6—Impact of water saturation and water memory on CO_2 consumption during hydrate formation

Given that the gas consumption rates decreased with increasing induction time, E3 exhibited the minimum CO_2 hydrate formation rate among the studied cases.

Determination of Water/Hydrate Saturations Using CT-Scan

Medical X-ray CT scans were employed for three selected water saturation (24%, 35&, and 41%) to evaluate water/hydrate distribution and quantify saturation throughout the core length during the hydrate formation/dissociation process. Given the resolution of medical CT images, and considering the similarity in density of water and CO_2 hydrate, it is very difficult to distinguish between these two phases through CT scanning.

Fig. 7 displays the CT scans from 24.3% water saturation (E6), where the first section shows the fully saturated and dry core (background section). The three images located at the top left illustrate water saturation progress (water saturation change within the core sections during the water/N_2 co-injection). The remaining set of images in this figure depicts the pattern of water + hydrate saturation in three stages, including the conditions before and after hydrate formation, and after hydrate dissociation. In this figure, two high porosity zones are situated around 2.25cm and 14.5cm from the inlet, which are the locations of the pressure transducer (P_1) and the thermocouple (T_{core}), respectively. This increased porosity and permeability results in an accumulation of more water, leading to a higher saturation of hydrate within these core sections.

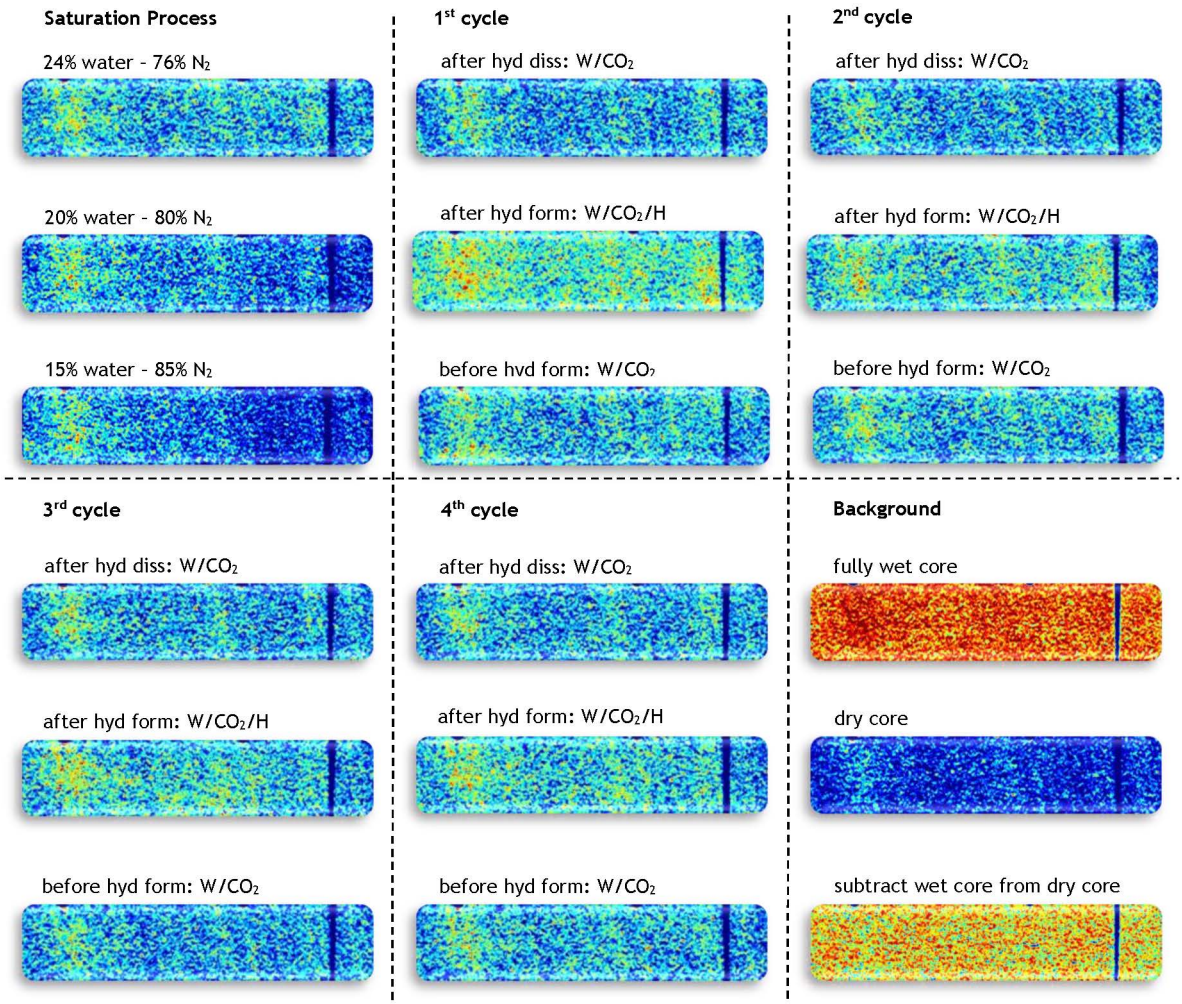

Figure 7—Dynamic CT images of water/hydrate saturation maps during the water saturation process of a horizontal Bentheimer rock sample as well as during hydrate formation/dissociation cycles in E6. flow direction is from left to right. (Colors qualitatively indicate water+hydrate saturation. red: high water/hydrate saturation; green/yellow: intermediate saturation; blue: low water/hydrate saturation)

Moreover, the CT images (Fig. 7) and the graph obtained from image analysis (Fig. 8) indicated a redistribution of water and hydrate along the core sections throughout hydrate growth, particularly in the third cycle (Y. Seol & T. J. Kneafsey, 2008). Furthermore, a comparison of water distribution across cycles confirmed that the hydrate dissociation process also altered the water distribution pattern. Based on Fig. 7, it is apparent that the hydrate saturation in the first cycle was slightly higher than the hydrate saturation observed in subsequent cycles. The observed slight decrease in hydrate saturation from the first cycle can be attributed to the influence of pore water redistribution on the rock surfaces (Vasheghani Farahani et al., 2021) and the possible evaporation of water into the gas phase. This redistribution impacts the likelihood of hydrate nucleation, particularly in areas where the local water saturation on the rock surface is higher (Rees et al., 2011). Another notable observation concluded from the cyclic tests on the Bentheimer core emphasizes the importance of the stochastic aspect of hydrate nucleation. Particularly under low subcooling conditions, serving as the hydrate driving force, hydrate nucleation is a stochastic process influenced by pore characteristics, salinity, and water history (Parent & Bishnoi, 1996; Servio & Englezos, 2003; Sloan, 1998). The experimental outcomes revealed that water level had the most significant impact on hydrate nucleation probability with 1wt% salinity under consistent thermal history (water memory). However, in reservoir conditions where multiple conflicting aspects come into play, hydrate nucleation may be controlled by several factors (Rees et al., 2011).

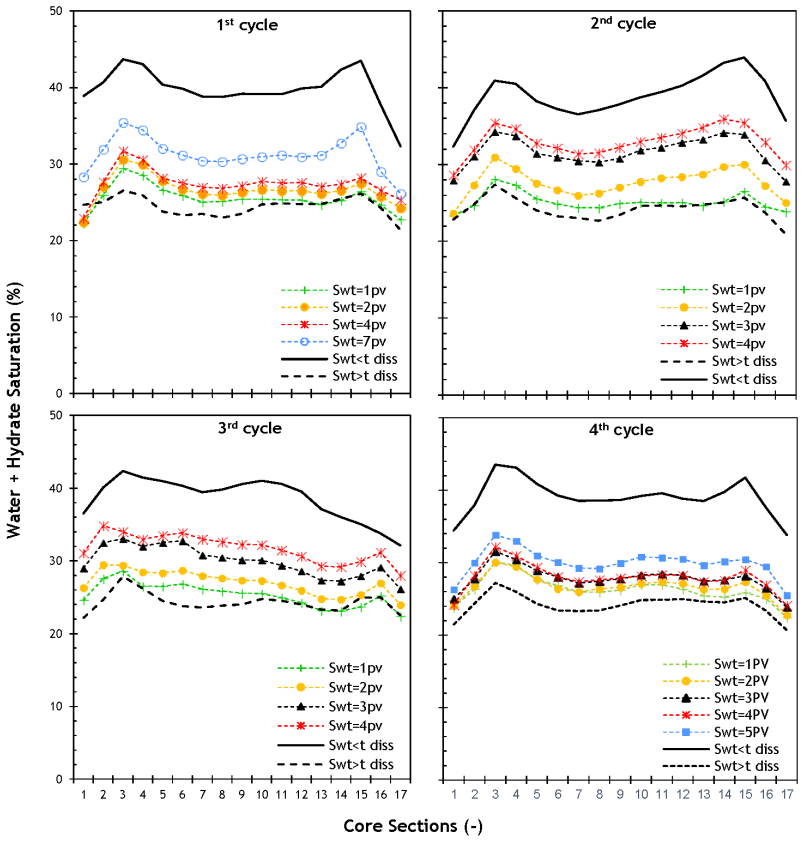

Figure 8—Slice average saturations of water/hydrate along the length of the core during CO_2 injection and hydrate formation/dissociation across multiple cycles in E6. The time scale PV is equivalent to 44min, based on the core pore volume and a CO_2 injection rate of 1 ml/min.

To visualize the growth patterns of CO_2 hydrate in Bentheimer sandstone in the presence/absence of water memory, hydrate was repeatedly formed under a constant temperature of 273.65K using medical CT scan. Images were taken throughout the stages of hydrate formation, during stable hydrate conditions lasting up to one day, and following the decomposition step. Fig. 8 shows the slice-average saturation of water/hydrate along the 17cm core during the four cycles of E6.

The data extracted from the CT scans of three selected water saturations are summarized in Table 2 and illustrated in Fig. 10. The results indicate an increase of approximately 10%~15% in final saturation of water+hydrate compared to the initial water saturation according to the flowchart represent in Fig. 9.

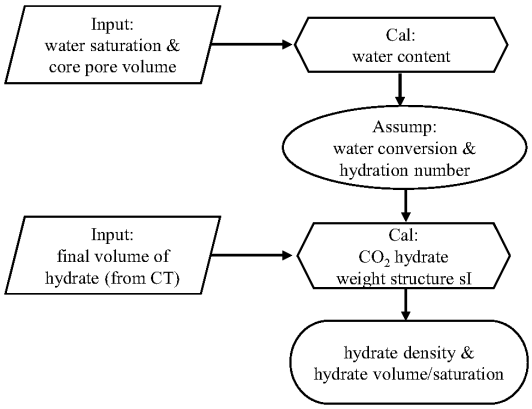

Figure 9—Procedure of the estimation and calculation method for hydrate density and hydrate volume/saturation calculation based on the CT scan results.

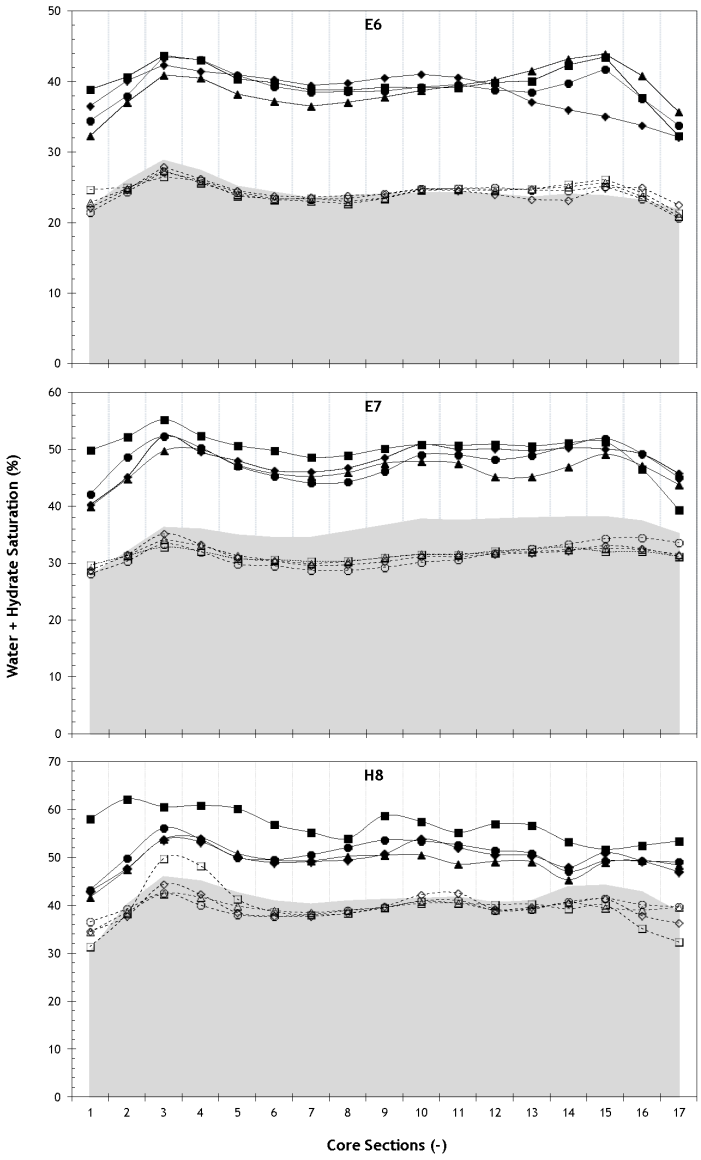

Figure 10—Steady state water + hydrate saturation profiles along the length of the Bernheimer Sandrock core during four cycles of CO_2 hydrate formation/decomposition in E6, 7, and 8. The solid area shows the initial level of water saturation. ▪: hydrate saturation of first cycle; ▲: hydrate saturation of second cycle; ♦: hydrate saturation of third cycle; ●: hydrate saturation of forth cycle; □; water saturation after CO_2 hydrate dissociation of first cycle; Δ: water saturation after CO_2 hydrate dissociation of second cycle ◊: water saturation after CO_2 hydrate dissociation of third cycle ○: water saturation after CO_2 hydrate dissociation of four cycle. (The solid line represents the CO_2 hydrate formation; The dashed line represents the CO_2 hydrate dissociation)

Furthermore, considering the hydraFLASH conversion results and that the final stage reached a steady state without any further volume increase, it has been determined that the maximum water-to-hydrate conversion exceeded 98%. Therefore, based on these findings, the density of hydrate emerged as a key factor. Under the specified experimental conditions, considering temperature, pressure, and excess CO_2 (due to the continuous CO_2 injection), HydraFLASH indicated a 21% water-to-hydrate conversion and a hydrate density of 0.803 g/ml with a hydration number ranging from ~5.9 to 6.1 for structure SI. However, the CT experimental results suggest that to achieve this specific density (0.803 g/ml), a higher hydration number (>6.7) is required. Consequently, the CT results imply that the hydrate cavities are semi-filled with CO_2, which provides valuable insights into the hydrate composition under the dynamic CO_2 injection.

In Table 2, besides confirming the random process of hydrate nucleation, the observed variations in induction times between cycles attributed to the changing water history during dissociation (Martinez

de Baños et al., 2015; Sefidroodi et al., 2013). For instance, in E7, hydrate was dissociated by thermal stimulation, and the core was kept at 293K for a minimum of 40 hours before fourth cycle of hydrate formation. These variations in thermal history are likely accountable for the discrepancies in induction time observed across the cycles. The results obtained indicate that induction times for CO_2 hydrate formation tend to increase with higher temperatures and longer dissociation durations.

The CO_2 injectivity index (J), calculated using Equation 8, which represents the ratio of the CO_2 injection rate $\left(q_{Co_2}\right)$ to the differential pressure (dp), is depicted in Fig. 11 for different experiments.

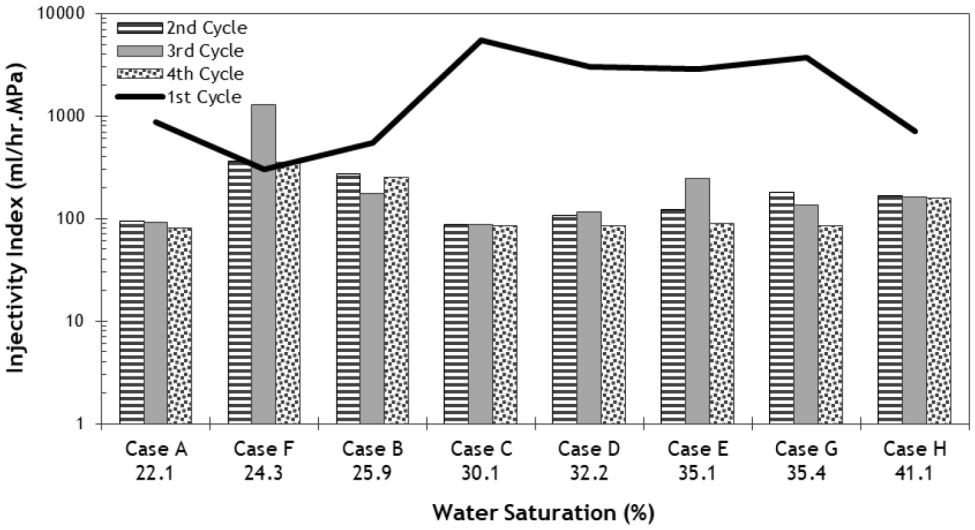

Figure 11—Injectivity index at initial rapid CO_2 consumption phase for different experiments.

$$J = \frac{q_{CO_2}}{dp} \tag{8}$$

This data compares the impact of water saturation on the CO_2 injectivity index at the beginning of the growth phase, where a substantial amount of CO_2 is consumed during CO_2 dissolution and hydrate generation (Gootam et al., 2021). Additionally, this figure highlights the effect of water memory on the injectivity of CO_2. The injectivity index during the hydrate growth phase in the first cycle of all experiments was higher compared to the following cycles. The experiment with an initial water saturation of 24.3% was an exception, suggesting that water memory had a minimal impact on the injectivity index, particularly during the third cycle. This deviation could be attributed to the fact that the volume/saturation of hydrate plays a role in influencing the injectivity index. According to the data reported in Table 2, the hydrate volume increased significantly due to hydrate growth in the first cycle of this particular test compared to other cycles. As a result, it was anticipated that the injectivity of the first cycle, even without considering water memory, would be lower than that of subsequent cycles (Wei & Maeda, 2023). Furthermore, in cycle 3 of this experiment (E6), the higher injectivity can be attributed to the fact that the duration of heating for hydrate dissociation exceeded one day. This prolonged duration ensured that all hydrate history was eliminated from the aqueous phase, contributing to the enhanced injectivity observed in this specific cycle (Kou et al., 2022; Li et al., 2021).

Permeability Change caused by Hydrate Formation

4. Two well-known Pang-Sharma model (Pang & Sharma, 1997) and Chen model (Chen et al., 2018) used to predict the permeability reduction as a function of hydrate (water). The Pang-Sharma model includes a constant (β) that accounts for trapped particles deposit in the pores presented in Equation 9:

$$\frac{k}{k_0} = \frac{1}{1+\beta s_H} \tag{9}$$

The Chen model proposes a modified Corey model which includes a fitting parameter (c) that is depicted in equation 10:

$$\frac{k}{k_0} = (1 - s_H)e^{-cs_H} \tag{10}$$

In above two equations the water permeability (k) values at each hydrate saturation were normalized by the initial permeability (k_0), the permeability before hydrate formation (Mahabadi et al., 2019). Our experimental results revealed decrease of normalized permeability with increase of water or hydrate saturation, as shown in Fig. 12. For hydrate saturations below 40%, the experimental findings align closely with the predicted values from the Pang-Sharma model, and include a tuning parameter (β=0.15) with a <0.03 mean deviation from the experimental data.

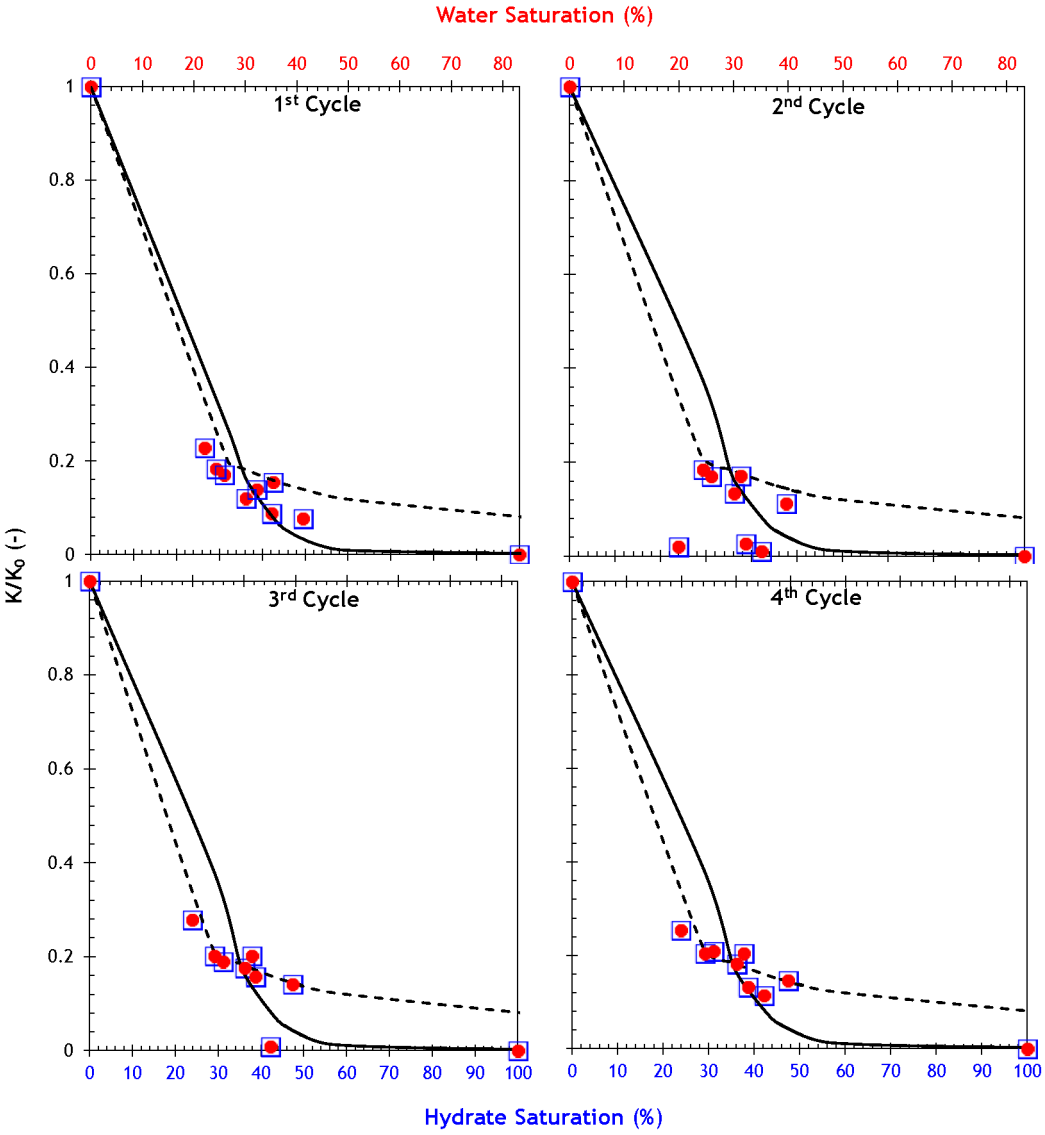

Figure 12—Normalized permeability as a function of water/hydrate saturation – a compilation of experimental data compared to Pang Sharma and Chen models. (The red solid circle are the normalized permeability as function of water saturation; the blue hollow squares are the normalized permeability as function of hydrate saturation; The dashed and solid lines correspond to the Pang-Sharma and Chen models respectively, with parameters adjusted using experimental data)

As illustrated in Fig. 12, the experimental results indicate a notable reduction in normalized permeability, approximately 80%, after hydrate formation across all water saturation levels. This permeability reduction was more pronounced at higher water saturation (up to 90%). However, the normalized permeability reduction resulting from CO_2 hydrate formation in porosity, driven by the memory effect, did not exhibit a significant change compared to the primary hydrate formation (first cycle without the memory effect). Furthermore, at some specific water saturations, e.g. 35% (second and third cycle) and 22.1% (second cycle), the primary flow channels were completely obstructed during some cycles. This blockage is attributed to alterations in water/hydrate distribution following previous hydrate dissociation. The observed significant decline in permeability highlights the profound impact of CO_2 hydrate formation on flow characteristics within porous media. This underscores the potential challenges and considerations inherent in CO_2 injection processes, especially when confronting the occurrence of complete blockage in flow channels during CO_2 injection. After conducting permeability tests with brine (1wt% NaCl) following CO_2 hydrate dissociation, a slight reduction in permeability was observed compared to the initial permeability (around ~2.5D). This reduction was attributed to salt dropout in some experiments, highlighting the influence of water memory on the salinity reduction during each hydrate formation/dissociation cycle. The observation arises from the fact that only water molecules enter the hydrate structure during formation, causing an increase in the salinity of the remaining brine. During hydrate dissociation, water molecules exit the lattice. However, due to limited mixing and a relatively slow rate of salt re-dissolution, the brine's salinity is effectively reduced during the following hydrate formation cycle. This reduction eventually leads to salt dropout or precipitation in the pores, impacting the pore permeability of sandstone (Roels et al., 2016). Moreover, the decrease in salinity enhances CO_2 solubility in brine, promoting hydrate formation in subsequent cycles.

Conclusions

This research focuses on investigating the impact of water saturation and water memory on saturation and kinetics of CO_2 hydrate in porous media under dynamic CO_2 injection conditions. The study employs five distinct water saturations ranging from 20% to 40% each of which contains four cycles of hydrate formation/dissociation. The core flood experiments are conducted at 273.65 K and an initial pressure of 3 MPa, under a medical CT scan to monitor the onset of hydrate formation and dynamics of hydrate growth inside the core, allowing for the calculation of hydrate saturation profiles. The key findings include:

- Direct correlation between CO_2 hydrate saturation and increasing water saturation levels.
- Increasing the rate and total amount of water-to-hydrate conversion in the presence of water memory, confirming the existence of the water memory effect in porous media.
- Substantial permeability reduction (approximately 80%), depending on the initial water saturation, as a result of hydrate formation at each water saturation. However, the generated hydrate is insufficient to completely block the CO_2 flow path.
- Increasing the volume of water+hydrate phases during hydrate formation, indicating a lower density for CO_2 hydrate compared to water. The estimated CO_2 hydrate density is reasonably consistent with data obtained from HydraFLASH software.

Acknowledgement

Authors thank Shell Global Solutions International for granting permission to publish this work.

Nomenclature

BP	Back Pressure
c	Chen model constant

CCS	Carbon Capture and Storage
CH	Core Holder
CP	Confining Pressure
CPA	Cubic-Plus-Association
CT	Computed Tomography
CT_{dry}	CT number of dry core [HU]
CT_{exp}	CT number during experiment [HU]
CT_{wet}	CT number of fully wet core [HU]
DP	Differential Pressure
E	Experiment
EoS	Equation of State
F_{conv}	water conversion [%]
JTC	Joule-Thomson Cooling
k	permeability [D]
MeOH	Methanol
MFC	Mass Flow Controller
m_H	mass of hydrate [g]
Mw	molecular weight [g/mol]
NH	hydration number
n	number of moles [mol]
n_t	moles of CO_2 at time t [mol]
n_{H_2O}	total mole of water [mol]
P	pressure
PT	Pressure Transducer
R	universal gas constant
r_{CO_2}	CO_2 consumption rate [mole/min]
S_H	hydrate saturation [%]
S_w	water saturation [%]
t	time [s]
T	Temperature
TC	Thermocouple
TJ	Thermal Jacket
V	Volume, [ml]
V_H	volume of hydrate [ml]
V_φ	volume of core porosity [ml]
z	compressibility factor

Greek Character

β	Pang-Sharma model constant
φ	porosity
ρ	density of hydrate [g/ml]
Δ	difference

Subscript & Superscript

H	hydrate
inj	injection
m	mole

t time
w water

References

Aghajanloo, M., Yan, L., Berg, S., Voskov, D., Farajzadeh, R.. (2023). Impact of CO_2 Hydrates on Injectivity During CO_2 Storage in Depleted Gas Fields: A Literature Review. *Gas Science and Engineering Journal*. https://doi.org/http://dx.doi.org/10.2139/ssrn.4674558

Akindipe, D., Saraji, S., & Piri, M. (2022). Salt precipitation in carbonates during supercritical CO2 injection: A pore-scale experimental investigation of the effects of wettability and heterogeneity. *International Journal of Greenhouse Gas Control*, **121**, 103790. https://doi.org/https://doi.org/10.1016/j.ijggc.2022.103790

Bachu, S. (2000). Sequestration of CO2 in geological media: criteria and approach for site selection in response to climate change. *Energy Conversion and Management*, **41**(9), 953–970. https://doi.org/https://doi.org/10.1016/S0196-8904(99)00149-1

Benson, S. M., & Cole, D. R. (2008). CO2 Sequestration in Deep Sedimentary Formations. *Elements*, **4**(5), 325–331. https://doi.org/10.2113/gselements.4.5.325

Boon, M., & Hajibeygi, H. (2022). Experimental characterization of $$(\text (H))_2$$/water multiphase flow in heterogeneous sandstone rock at the core scale relevant for underground hydrogen storage (UHS). *Scientific Reports*, **12**(1), 14604. https://doi.org/10.1038/s41598-022-18759-8

Chen, X., Verma, R., Espinoza, D. N., & Prodanović, M. (2018). Pore-scale determination of gas relative permeability in hydrate-bearing sediments using X-ray computed micro-tomography and lattice Boltzmann method. *Water Resources Research*, **54**(1), 600–608.

Chesnokov, C., A. F. Rouhi and Kahrobaei, Siavash and Snippe, Jeroen and Bedrikovetski, Pavel, (2023). Analytical Model for Joule-Thomson Cooling Under Heat Exchange During Co2 Storage in Geological Formations. SSRN. https://doi.org/http://dx.doi.org/10.2139/ssrn.4441293

Dance, T. (2013). Assessment and geological characterisation of the CO_2CRC Otway Project CO_2 storage demonstration site: From prefeasibility to injection. *Marine and Petroleum Geology*, **46**, 251–269. https://doi.org/https://doi.org/10.1016/j.marpetgeo.2013.06.008

Dhamu, V., Qureshi, M. F., Abubakar, S., Usadi, A., Barckholtz, T. A., Mhadeshwar, A. B., & Linga, P. (2023). Investigating High-Pressure Liquid CO2 Hydrate Formation, Dissociation Kinetics, and Morphology in Brine and Freshwater Static Systems. *Energy & Fuels*, **37**(12), 8406–8420. https://doi.org/10.1021/acs.energyfuels.3c01089

Eftekhari, A. A., & Farajzadeh, R. (2017). Effect of Foam on Liquid Phase Mobility in Porous Media. *Scientific Reports*, **7**(1), 43870. https://doi.org/10.1038/srep43870

Farajzadeh, R., Chesnokov, C., Kahrobaei, S., Snippe, J., Bedrikovetski, P. (2023). Analytical Model for Joule-Thomson Cooling Under Heat Exchange During Co2 Storage in Geological Formations. SSRN. https://doi.org/http://dx.doi.org/10.2139/ssrn.4441293

Gauteplass, J., Almenningen, S., Barth, T., & Ersland, G. (2020). Hydrate Plugging and Flow Remediation during CO2 Injection in Sediments. *Energies*, **13**(17), 4511. https://www.mdpi.com/1996-1073/13/17/4511

Ge, B.-B., Zhong, D.-L., & Lu, Y.-Y. (2019). Influence of water saturation and particle size on methane hydrate formation and dissociation in a fixed bed of silica sand. *Energy Procedia*, **158**, 5402–5407. https://doi.org/https://doi.org/10.1016/j.egypro.2019.01.623

Gootam, D., Gaikwad, N., Kumar, R., & Kaisare, N. (2021). Modeling Growth Kinetics of Methane Hydrate in Stirred Tank Batch Reactors. *ACS Engineering Au*, **1**(2), 148–159. https://doi.org/10.1021/acsengineeringau.1c00012

Hansen, O., Gilding, D., Nazarian, B., Osdal, B., Ringrose, P., Kristoffersen, J.-B., Eiken, O., & Hansen, H. (2013). Snøhvit: The History of Injecting and Storing 1 Mt CO2 in the Fluvial Tubåen Fm. *Energy Procedia*, **37**, 3565–3573. https://doi.org/https://doi.org/10.1016/j.egypro.2013.06.249

Hoteit, H., Fahs, M., & Soltanian, M. R. (2019). Assessment of CO2 Injectivity During Sequestration in Depleted Gas Reservoirs. *Geosciences*, **9**(5), 199. https://www.mdpi.com/2076-3263/9/5/199

House, K. Z., Schrag, D. P., Harvey, C. F., & Lackner, K. S. (2006). Permanent carbon dioxide storage in deep-sea sediments. Proceedings of the National Academy of Sciences, **103**(33), 12291–12295. https://doi.org/doi:10.1073/pnas.0605318103

Ketzer, J. M., Iglesias, R. S., & Einloft, S. (2012). Reducing Greenhouse Gas Emissions with CO2 Capture and Geological Storage. In W.-Y. Chen, J. Seiner, T. Suzuki, & M. Lackner (Eds.), *Handbook of Climate Change Mitigation* (pp. 1405–1440). Springer US. https://doi.org/10.1007/978-1-4419-7991-9_37

Kou, X., Feng, J.-C., Li, X.-S., Wang, Y., & Chen, Z.-Y. (2022). Memory effect of gas hydrate: Influencing factors of hydrate reformation and dissociation behaviors☆. *Applied Energy*, **306**, 118015. https://doi.org/https://doi.org/10.1016/j.apenergy.2021.118015

Krevor, S. C. M., Pini, R., Zuo, L., & Benson, S. M. (2012). Relative permeability and trapping of CO2 and water in sandstone rocks at reservoir conditions. *Water Resources Research*, **48**(2). https://doi.org/https://doi.org/10.1029/2011WR010859

Le Goff, T. H., Lagarde, F., Thibeau, S., Brisset, A.. (2021). CO2 Injection in Depleted Reservoirs: Analysis, Modelling 15th Greenhouse Gas Control Technologies Conference

Lei, L., & Seol, Y. (2019). High-Saturation Gas Hydrate Reservoirs—A Pore Scale Investigation of Their Formation From Free Gas and Dissociation in Sediments. *Journal of Geophysical Research: Solid Earth*, **124**. https://doi.org/10.1029/2019JB018243

Li, Y., Wu, N., He, C., Sun, Z., Zhang, Z., Hao, X., Chen, Q., Bu, Q., Liu, C., & Sun, J. (2021). Nucleation probability and memory effect of methane-propane mixed gas hydrate. *Fuel*, **291**, 120103. https://doi.org/https://doi.org/10.1016/j.fuel.2020.120103

Mahabadi, N., Dai, S., Seol, Y., & Jang, J. (2019). Impact of hydrate saturation on water permeability in hydrate-bearing sediments. *Journal of Petroleum Science and Engineering*, **174**, 696–703. https://doi.org/https://doi.org/10.1016/j.petrol.2018.11.084

Martinez de Baños, M. L., Carrier, O., Bouriat, P., & Broseta, D. (2015). Droplet-based millifluidics as a new tool to investigate hydrate crystallization: Insights into the memory effect. *Chemical Engineering Science*, **123**, 564–572. https://doi.org/https://doi.org/10.1016/j.ces.2014.11.018

Nunes, L. J. R. (2023). The Rising Threat of Atmospheric CO2: A Review on the Causes, Impacts, and Mitigation Strategies. *Environments*, **10**(4), 66. https://www.mdpi.com/2076-3298/10/4/66

Oldenburg, C. (2006). Joule-Thomson cooling due to CO2 injection into natural gas reservoirs. *Lawrence Berkeley National Laboratory*, **48**. https://doi.org/10.1016/j.enconman.2007.01.010

Oldenburg, C. M., & Benson, S. M. (2002). CO2 Injection for Enhanced Gas Production and Carbon Sequestration. SPE International Petroleum Conference and Exhibition in Mexico

Pang, S., & Sharma, M. M. (1997). A Model for Predicting Injectivity Decline in Water-Injection Wells. *SPE Formation Evaluation*, **12**(03), 194–201. https://doi.org/10.2118/28489-pa

Parent, J., & Bishnoi, P. (1996). Investigations into the nucleation behaviour of methane gas hydrates. *Chemical Engineering Communications*, **144**(1), 51–64.

Rees, E. V. L., Kneafsey, T. J., & Seol, Y. (2011). Methane Hydrate Distribution from Prolonged and Repeated Formation in Natural and Compacted Sand Samples: X-Ray CT Observations. *Journal of Geological Research*, **2011**, 791815. https://doi.org/10.1155/2011/791815

Rodger, P. M. (2000). Methane hydrate: melting and memory. *Annals of the New York Academy of Sciences*, **912**(1), 474–482.

Roels, S. M., El Chatib, N., Nicolaides, C., & Zitha, P. L. J. (2016). Capillary-Driven Transport of Dissolved Salt to the Drying Zone During $$\hbox {CO}_{2}$$Injection in Homogeneous and Layered Porous Media. *Transport in Porous Media*, **111**(2), 411–424. https://doi.org/10.1007/s11242-015-0601-y

Roy, P., Mohanty, A., & Misra, M. (2023). Prospects of carbon capture, utilization and storage for mitigating climate change. *Environmental Science: Advances*, 2. https://doi.org/10.1039/D2VA00236A

Sefidroodi, H., Abrahamsen, E., & Kelland, M. A. (2013). Investigation into the strength and source of the memory effect for cyclopentane hydrate. *Chemical Engineering Science*, **87**, 133–140. https://doi.org/https://doi.org/10.1016/j.ces.2012.10.018

Seol, Y., & Kneafsey, T. (2008). FLUID FLOW THROUGH HETEROGENEOUS METHANE HYDRATE BEARING SAND: OBSERVATIONS USING X-RAY CT SCANNING.

Servio, P., & Englezos, P. (2003). Morphology of methane and carbon dioxide hydrates formed from water droplets. *AIChE journal*, **49**(1), 269–276.

Singh, R. P., Shekhawat, K. S., Das, M. K., & Muralidhar, K. (2020). Geological sequestration of CO2 in a water-bearing reservoir in hydrate-forming conditions. *Oil Gas Sci. Technol. – Rev. IFP Energies nouvelles*, **75**, 51. https://doi.org/10.2516/ogst/2020038

Sloan, E. D. (1998). Clathrate Hydrates of Natural Gases, Second Edition, Revised and Expanded. Taylor & Francis. https://books.google.nl/books?id=jBaLcv6qKnsC

Sloan, E. D., Subramanian, S., Matthews, P., Lederhos, J., & Khokhar, A. (1998). Quantifying hydrate formation and kinetic inhibition. *Industrial & engineering chemistry research*, **37**(8), 3124–3132.

Sun, D., & Englezos, P. (2016). CO2 storage capacity in laboratory simulated depleted hydrocarbon reservoirs – Impact of salinity and additives. *Journal of Natural Gas Science and Engineering*, **35**, 1416–1425. https://doi.org/https://doi.org/10.1016/j.jngse.2016.03.043

Thompson, H., Soper, A. K., Buchanan, P., Aldiwan, N., Creek, J. L., & Koh, C. A. (2006). Methane hydrate formation and decomposition: Structural studies via neutron diffraction and empirical potential structure refinement. *The Journal of Chemical Physics*, **124**(16).

Underschultz, J., Boreham, C., Dance, T., Stalker, L., Freifeld, B., Kirste, D., & Ennis-King, J. (2011). CO_2 storage in a depleted gas field: An overview of the CO_2CRC Otway Project and initial results. *International Journal of Greenhouse Gas Control - INT J GREENH GAS CONTROL*, **5**, 922–932. https://doi.org/10.1016/j.ijggc.2011.02.009

Vasheghani Farahani, M., Guo, X., Zhang, L., Yang, M., Hassanpouryouzband, A., Zhao, J., Yang, J., Song, Y., & Tohidi, B. (2021). Effect of thermal formation/dissociation cycles on the kinetics of formation and pore-scale distribution of methane hydrates in porous media: a magnetic resonance imaging study [10.1039/D0SE01705A]. *Sustainable Energy & Fuels*, **5**(5), 1567–1583. https://doi.org/10.1039/D0SE01705A

Wang, J., Tie, Y., Liu, Z., Zhang, L., Jiang, H., & Guo, P. (2022). Effects of Different Factors on Methane Hydrate Formation Using a Visual Wellbore Simulator. *ACS Omega*, **7**(27), 23147–23155. https://doi.org/10.1021/acsomega.2c00903

Wang, L., Dou, M., Wang, Y., Xu, Y., Li, Y., Chen, Y., & Li, L. (2022). A Review of the Effect of Porous Media on Gas Hydrate Formation. *ACS Omega*, **7**(38), 33666–33679. https://doi.org/10.1021/acsomega.2c03048

Wapperom, M., Lyu, X., & Voskov, D. (2022). Accurate Modeling of Near-Wellbore Effects Induced by Supercritical CO2 Injection. **2022**(1), 1–13. https://doi.org/https://doi.org/10.3997/2214-4609.202244092

Wei, Y., & Maeda, N. (2023). Mechanisms of the memory effect of clathrate hydrates. *Chemical Engineering Science*, **270**, 118538. https://doi.org/https://doi.org/10.1016/j.ces.2023.118538

Wells, J. D., Majid, A. A. A., Creek, J. L., Sloan, E. D., Borglin, S. E., Kneafsey, T. J., & Koh, C. A. (2020). Water content of carbon dioxide at hydrate forming conditions. *Fuel*, **279**, 118430. https://doi.org/https://doi.org/10.1016/j.fuel.2020.118430

Wen, Z., Yao, Y., Luo, W., & Lei, X. (2021). Memory effect of CO2-hydrate formation in porous media. *Fuel*, **299**, 120922. https://doi.org/https://doi.org/10.1016/j.fuel.2021.120922